Supplementary information:

Temperature-independent thermal radiation

Alireza Shahsafi[1*], Patrick Roney[1*], You Zhou[2], Zhen Zhang[3], Yuzhe Xiao[1], Chenghao Wan[1,4], Raymond Wambold[1], Jad Salman[1], Zhaoning Yu[1,5], Jiarui Li[6], Jerzy T. Sadowski[7], Riccardo Comin[6], Shriram Ramanathan[3], and Mikhail A. Kats[1,4,5†]

[1]Department of Electrical and Computer Engineering, University of Wisconsin – Madison, Madison, Wisconsin
[2]School of Engineering and Applied Sciences, Harvard University, Cambridge, Massachusetts
[3]School of Materials Engineering, Purdue University, West Lafayette, Indiana
[4]Materials Science and Engineering, University of Wisconsin – Madison, Madison, Wisconsin
[5]Department of Physics, University of Wisconsin – Madison, Madison, Wisconsin
[6]Department of Physics, Massachusetts Institute of Technology, Cambridge, MA
[7]Center for Functional Nanomaterials, Brookhaven National Laboratory, Upton, New York

* These authors contributed equally
† Correspondence to mkats@wisc.edu

1. Zero-differential thermal emission cannot be achieved based on hysteretic phase-change materials

In the main text, we defined a zero-differential thermal emitter (ZDTE) as an object that emits with power P, such that $\partial P/\partial T = 0$ over a prescribed temperature range. When the emitted power considered is over all wavelengths, this condition occurs when the total (integrated) emissivity has the form of $\varepsilon_{tot} = \gamma T^{-4}$, where γ is a constant with units of K^4. Here, there is clearly a one-to-one relationship between ε_{tot} and temperature T. This also remains the case when a limited range of wavelengths is considered (in the main text, from 8 μm to 14 μm), though the exact form of the emissivity will be slightly modified.

Because a one-to-one relationship is required, any temperature-dependent material that has hysteresis (i.e., can have the same optical properties for two different temperatures) cannot be used to realize a ZDTE. As an example of this, we simulated a structure comprising a 150-nm-thick film of vanadium dioxide (VO_2), a phase-transition material with optical properties that change strongly as a function of temperature nears its insulator-to-metal transition close to 70 °C. Using the optical properties of VO_2 [S1] and the transfer matrix method [S2], we calculated the thermal emission of 150-nm-thick film of VO_2 on sapphire in Fig. S1.

In Fig. S1, there do exist several temperatures at which $\partial P/\partial T = 0$. However, these temperatures are not the same between the heating and cooling cycles due to the hysteresis present in VO_2. In contrast, the $SmNiO_3$ used in the main text has negligible hysteresis and can therefore be used to realize the ZDTE condition.

www.pnas.org/cgi/doi/10.1073/pnas.1911244116

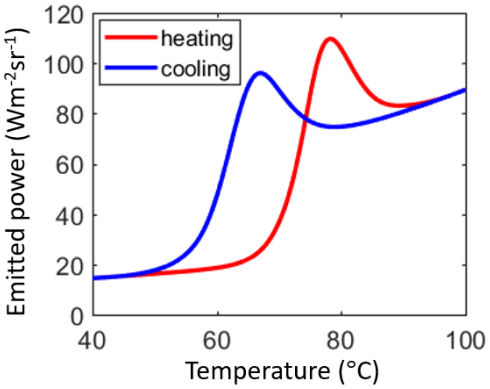

Figure S1. Calculated emitted power for a 150-nm-thick VO_2 film on a sapphire substrate. The hysteretic insulator-metal transition renders the system not suitable for realization of ZDTE.

2. Temperature-dependent reflectance characterization and cycling tests

To ensure that the optical response of $SmNiO_3$ has no hysteresis, we performed temperature-dependent reflection measurements for a full cycle of heating and cooling [Fig. S2(a-b)] on the same $SmNiO_3$/sapphire sample used for the main text. Various temperature-dependent optical measurements have been performed several times over a period of approximately two years, with no apparent degradation of the samples.

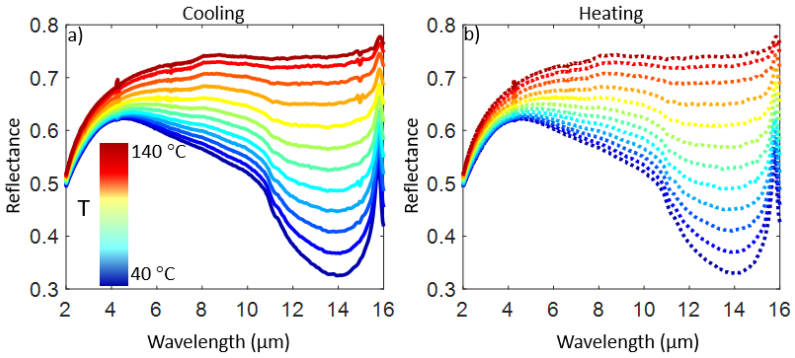

Figure S2. Measured reflectance of the sample used for the main text taken under both **(a)** cooling and **(b)** heating. We observed no hysteresis (see also Fig. 2(a, b) in the main text).

To further investigate the stability of our $SmNiO_3$ films, we also analyzed a different sample grown under the same conditions, consisting of a ~200-nm film of $SmNiO_3$ on an $LaAlO_3$ substrate [inset of Fig. S3(a)]. No substantial differences in $SmNiO_3$ quality or degradation was observed between the two substrates ($LaAlO_3$ vs. sapphire). We performed temperature-dependent reflection measurements on this sample and thermally drove it between the two phases every few minutes. The reflectances at different wavelengths [Fig. S3(c-f)] shows that the optical response of the film is stable and has no memory over many cycles, as was expected from the literature [S3-S4].

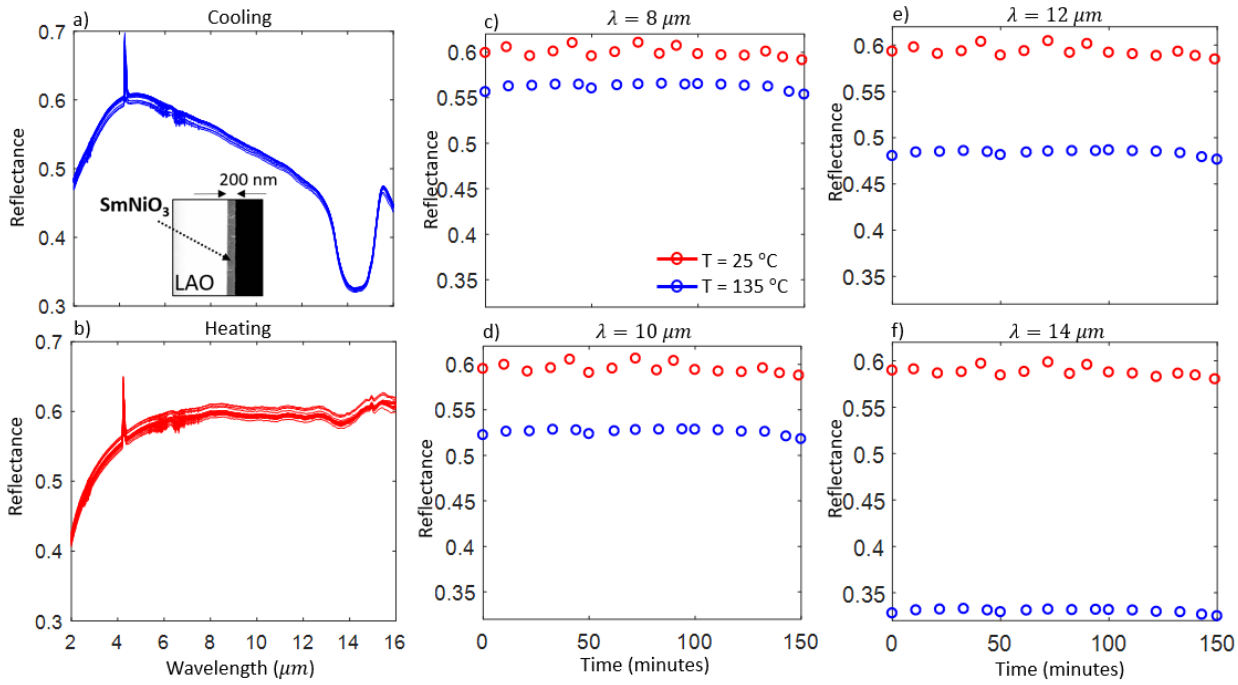

Figure S3. Reflectance of ~200-nm $SmNiO_3$ on an $LaAlO_3$ substrate across the $SmNiO_3$ phase transition during **(a)** heating and **(b)** cooling. The inset shows a cross-sectional image of the sample. We thermally cycled the sample between 25 and 135 °C many times every two minutes for 150 minutes. The sharp peak is a result of atmospheric (CO_2) absorption. Panels **(c-f)** show the reflectance at several different wavelengths (λ = 8, 10, 12, and 14 μm).

3. Temperature-dependent X-ray diffraction (XRD)

X-ray diffraction (XRD) measurements were carried out on an $SmNiO_3$ thin film deposited on a sapphire substrate, shown in Fig. 1. A wide-range XRD profile [Fig. S4(a)] shows clear diffraction peaks from orthorhombic $SmNiO_3$. Diffraction peaks from various planes are observed from $SmNiO_3$, indicating that this $SmNiO_3$ film possesses polycrystalline structure, as expected. To investigate the structural evolution of $SmNiO_3$ across the IMT, the diffraction peak from the (110)/(002) planes of $SmNiO_3$ was measured *in-situ* upon heating [Fig. S4(b)]. No obvious shift of the diffraction peak from $SmNiO_3$ appears upon heating to 200 °C, which is consistent with the high-resolution neutron diffraction measurements reported previously [S5]. As expected, the IMT of $SmNiO_3$ is not driven by large lattice distortions but rather very subtle bond distortions [S5], which may contribute to its hysteresis-free and gradual phase-change features observed in optical and electrical measurements. The lattice parameter change due to thermal expansion is within the resolution of the laboratory XRD and hence is a very subtle change.

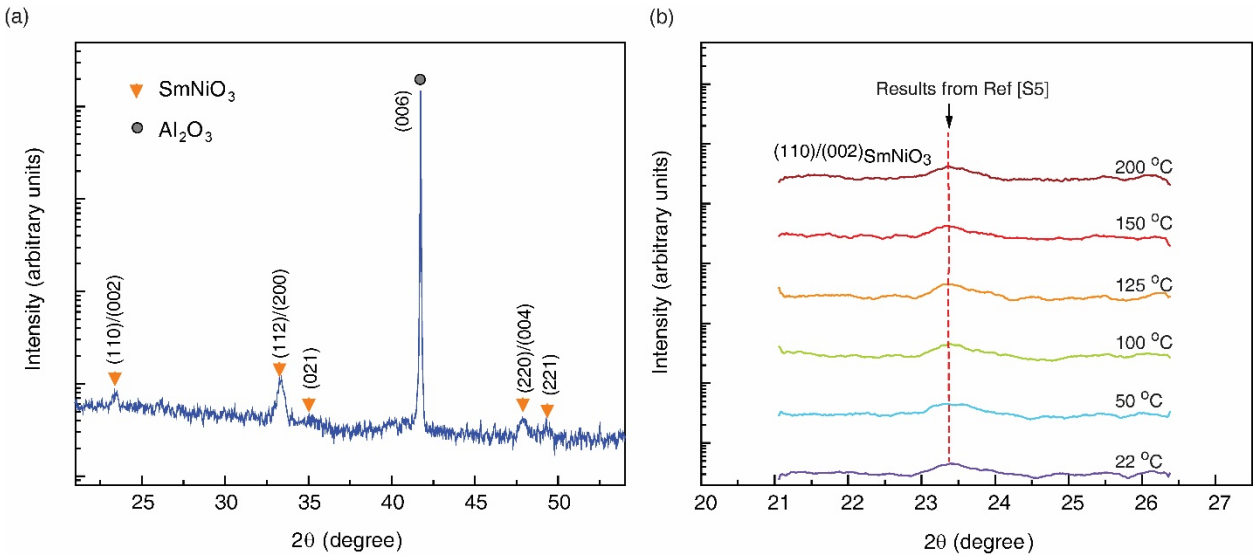

Fig. S4. *In-situ* XRD measurement of an $SmNiO_3$ thin film deposited on a sapphire substrate. (a) XRD profile of an $SmNiO_3$ thin film measured at room temperature, where the diffraction peaks from $SmNiO_3$ and the sapphire (Al_2O_3) substrate are indicated. (b) In-situ XRD profile of the (110)/(002) diffraction peak of $SmNiO_3$ upon heating. The red dashed line indicates the extracted 2θ value of $SmNiO_3$ from neutron powder diffraction reported in Ref [S5].

4. Comparison of ZDTE performance for $SmNiO_3$ on sapphire and $LaAlO_3$

Based on the characterized complex refractive index of $SmNiO_3$ and the optical properties of sapphire and $LaAlO_3$ from literature [S6], we estimated the ZDTE performance of $SmNiO_3$ films of different thickness on these two substrates. Our calculations show that both substrates work well, but slightly superior performance is achieved with the sapphire substrate (Fig. S5).

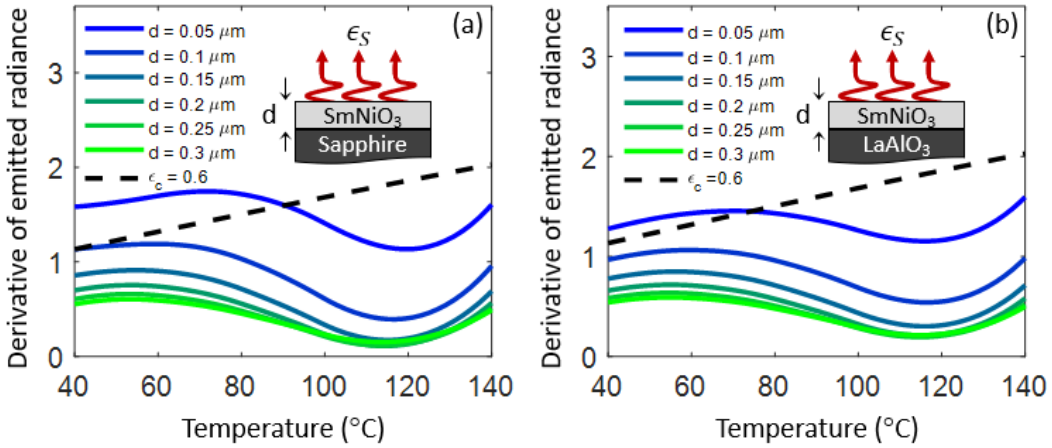

Figure S5. Calculated temperature derivative of the emitted radiance of an $SmNiO_3$ film with thickness d from 50 nm to 300 nm on (a) sapphire and (b) $LaAlO_3$ substrates. The dashed line yields the calculated radiance from a temperature-independent reference with a constant emissivity of 0.6.

5. X-ray absorption spectroscopy (XAS) and x-ray photoemission electron microscopy (XPEEM)

Nanoscale x-ray absorption spectroscopy (XAS) and x-ray photoemission electron microscopy (XPEEM) has been used to image the metallic and insulating phase co-existence in the nickelate family [S7]. We performed XAS and XPEEM measurements on an epitaxial $SmNiO_3$ (001) thin film grown on a $LaAlO_3$ substrate and observed no spatial features above the detector noise level. The spatially averaged XAS shows a disappearance of the double-peak structure near the Ni-L3 absorption edge across the IMT, corresponding to the melting of charge disproportionation (Fig. S6). The ratio of the absorption coefficients at 848 and 849 eV [$r = XAS\ (848\ eV)\ /\ XAS\ (849\ eV)$] is 1.02 in the insulating phase and 0.98 in the metallic phase. This value can therefore be used as a proxy for spatial identification of the local electronic state. The spatial mapping of the parameter r can be obtained from the pixel-by-pixel ratio of two XPEEM images taken at 848 and 849 eV. Spatial maps of $r(x, y)$ over a field of view of 15 µm diameter are shown in Fig. S7, underscoring the absence of any domain texture or phase coexistence beyond the noise level, even for a temperature (120 °C) deep within the IMT.

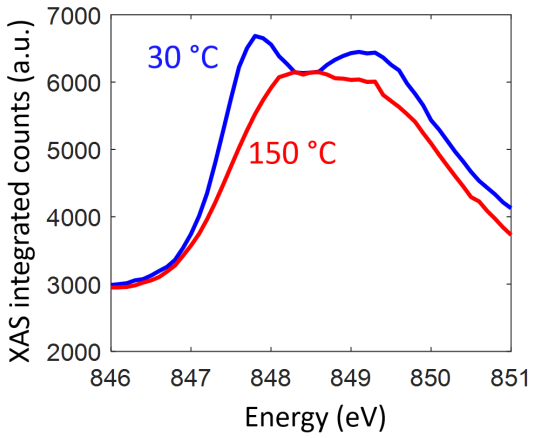

Figure S6. Spatially averaged X-ray absorption spectra of $SmNiO_3$ (001) on an $LaAlO_3$ substrate at temperatures below and above the IMT. The XAS near the Ni L3 edge changes peak shape across the MIT transition. The ratio of the values at the two energies identified in the diagram is XAS(848)/XAS(849) = 1.02 at 30 °C and 0.98 at 150 °C.

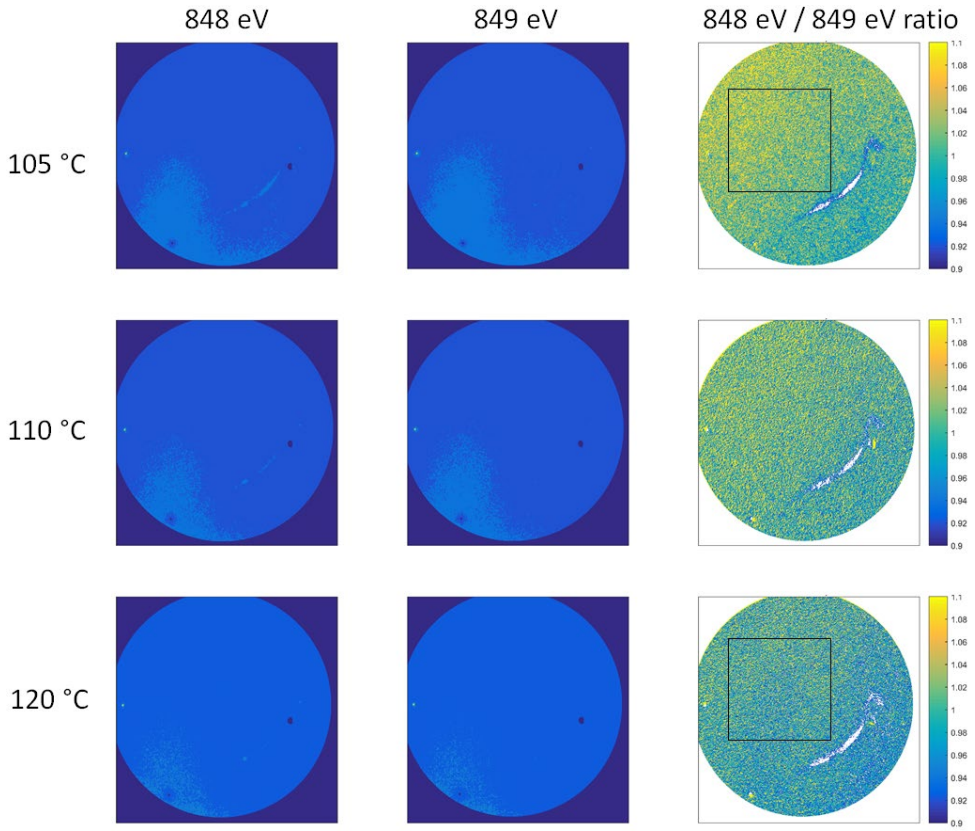

Figure S7. Left: XPEEM images of the same sample as in Fig. S4, at 848 eV and 849 eV. Images were taken with the same field of view, by aligning to surface defects and scratches. The color scale is normalized to the min and max of each map. Right: ratio between the 848 and 849 eV absorption maps. Data was acquired for three different temperatures throughout the IMT. The field of view (i.e., diameter of the circular aperture) is 15 μm. The maps have no recognizable spatial features other than a surface scratch on the detector (visible on the right), and detector noise.

6. Algorithm for extracting emissivity from direct-emission measurements

In general, one can describe the detected emission signal from an FTIR system as [S8]:

$$S_X(\lambda,T) = m(\lambda)[L_{BB}(\lambda,T)\varepsilon_X(\lambda,T) + B_X(\lambda,T)] \tag{S3-1}$$

where $S_X(\lambda,T)$ is the measured Fourier-transformed emission spectrum, $m(\lambda)$ is the system response, $\varepsilon_X(\lambda,T)$ is the temperature-dependent sample emissivity, $L_{BB}(\lambda,T)$ is the blackbody radiance, and $B_X(\lambda,T)$ is the background, which can also be sample dependent. To calibrate our FTIR, we performed temperature-dependent thermal-emission measurements using three samples: a vertically-aligned carbon nanotube forest (CNT) [S9] "blackbody" (with constant $\varepsilon \sim 0.95$ across the infrared spectral range), a fused-silica wafer, and a sapphire wafer.

Using Eq. (S3-1) and further analysis of our FTIR instrument [S10], we can obtain the emissivity of an unknown sample from a known reference α via:

$$\varepsilon_X(\lambda,T) = \varepsilon_\alpha(\lambda,T)\,\frac{S_X(\lambda,T)}{S_\alpha(\lambda,T)} \tag{S3-2}$$

Note that S3-2 does not work for all situations and systems; careful analysis is necessary to make sure that the emissivity is being extracted correctly. We measured the emissivity of our test samples (polished fused silica and sapphire wafers) by using this formula, and further confirmed that the extracted emissivity matches well with the value obtained by spectroscopic ellipsometry, Fresnel equations, and an application of Kirchhoff's law (Fig. 3(a) in ref. [S10]).

7. Angular response of our ZDTE

We numerically studied the angular dependence of the thermal radiance of our $SmNiO_3$/sapphire ZDTE. Based on our numerical analysis [Fig. S8(a-b)], the ZDTE effect persists for p-polarized emission up to an emission angle of about 40°, and for s-polarized emission for essentially every angle. Averaging the polarizations, the effect persists up to about 60° [Fig. S8(c)]. In our calculations, we incorporated the optical anisotropy in the sapphire substrate [S11] by using the transfer matrix method [S2], with the Fresnel coefficients generalized for birefringent media [S12]. The refractive indices of $SmNiO_3$ that we used were extracted by ellipsometry analysis, assuming that they were isotropic [Fig. 2(c, d)].

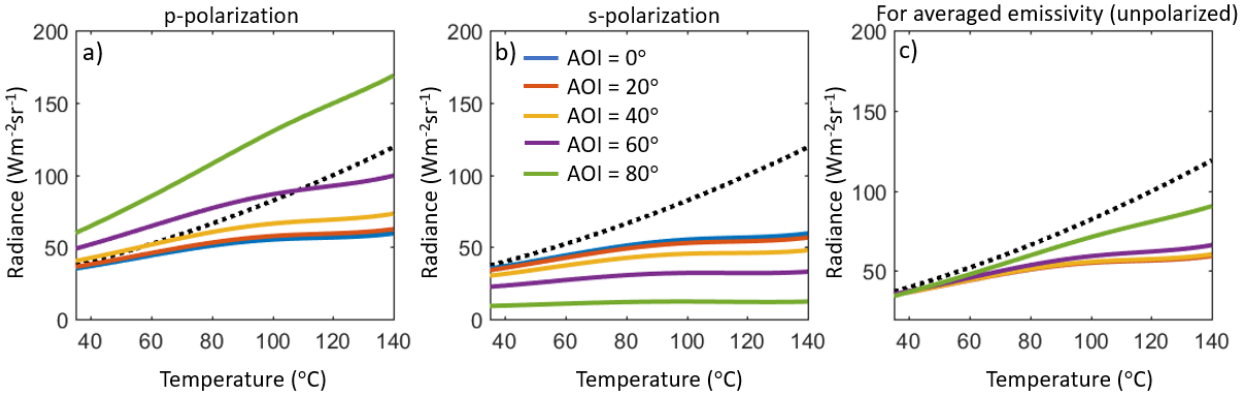

Figure S8. Calculated radiance versus temperature and angle for the structure characterized in Fig. 3(a) of the main text for **(a)** p-polarized, **(b)** s-polarized, and **(c)** polarization-averaged emissivity.

8. Temperature drop between the bottom and top surfaces of the substrate

Here, we provide our numerical analysis of the temperature drop due to the non-zero thermal conductivity and thickness of our emitter. We calculated the temperature distribution for a 0.5-mm-thick sapphire sitting on top of a 100 °C heater surface [Fig. S9(a)]. For this calculation, we solved one-dimensional heat equation ($\frac{\partial T(t,z)}{\partial t} = \frac{k}{\rho C_p}\frac{\partial^2 T(t,z)}{\partial z^2}$) along the sapphire wafer using the heat transfer parameters for sapphire from Table 1. From this calculation, we find out that the temperature drop is 0.02 °C.

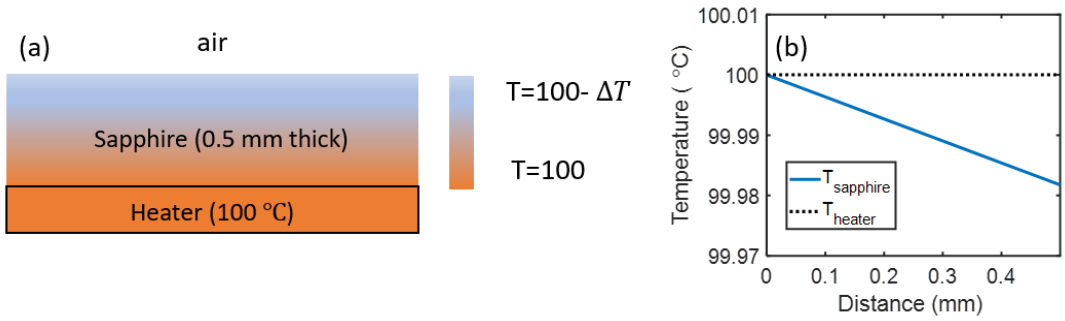

Figure S9. **(a)**: schematic of the heat-transfer simulation. **(b)** calculated steady state temperature profile for a 1-mm-thick sapphire on top of a 100 ℃ heater surface.

Table 1. Heat-transfer parameters for sapphire

k (W/(m· ℃))	ρ (g/cm^3)	C_p (J/(kg· ℃))
24*	3.98	760

*The thermal conductivity is chosen to be the average value of perpendicular and parallel to the c-axis, though we note that the values are very close to each other.

9. Extending the temperature range of ZDTE

In this section, we show that it may be possible to achieve ZDTE over a different temperature range than what we demonstrated in the paper by leveraging other rare-earth nickelates with lower transition temperatures. As shown in Ref. [S4], while the transition temperatures of $SmNiO_3$ and neodymium nickelate ($NdNiO_3$) are roughly 100 and −100 °C, respectively, $Sm_{0.75}Nd_{0.25}NiO_3$ has a transition temperature between these extremes [Fig. S10(a)]. While the optical properties of this or similar quaternary alloys have not yet been reported in the literature, the similarity in electrical behavior demonstrated in Fig. 1 of ref. [S4] suggests that the optical properties show some parallels to that of $SmNiO_3$. Therefore, we designed and simulated a zero-differential emitter for the temperature range of 45 to 80 °C using a 250-nm-thick $Sm_{0.75}Nd_{0.25}NiO_3$ thin film on a sapphire substrate, making the assumption that this alloy has the same spectral optical properties as $SmNiO_3$, but with a transition temperature 50 °C smaller than that of $SmNiO_3$. The calculated ZDTE effect is shifted to a temperature range centered at 60 °C [Fig. S10(b)].

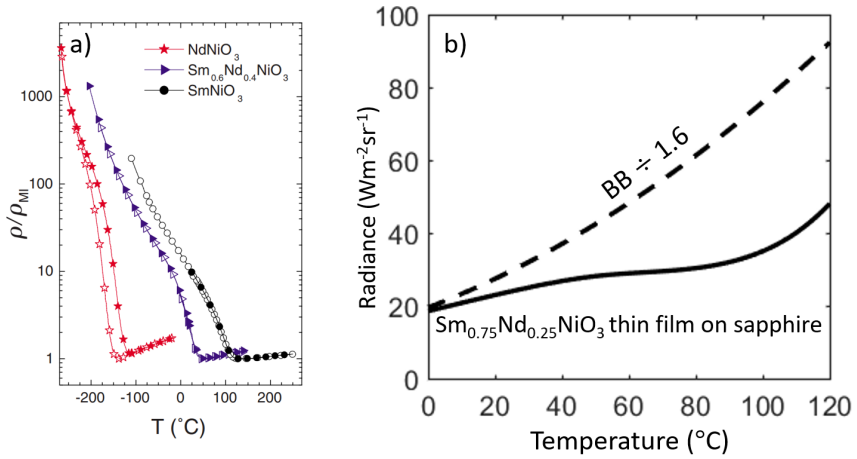

Figure S10. (a) Resistivity versus temperature for different rare-earth nickelates, including one quaternary alloy. This panel is reprinted from ref. [S4] with permission from APS. (b) Calculated emitted radiance for a 250-nm-thick $Sm_{0.75}Nd_{0.25}NiO_3$ thin film on sapphire, assuming that the $Sm_{0.75}Nd_{0.25}NiO_3$ film has the same optical properties as $SmNiO_3$ but with the transition temperature 50° lower than that of $SmNiO_3$.

Supplementary references

[S1] Wan, C., et al. (2019). Optical properties of thin-film vanadium dioxide from the visible to the far infrared. *Annalen der Physik,* 531(10), 1900188.

[S2] Byrnes, S. (2016). Multilayer optical calculations, arXiv:1603.02720.

[S3] Ha, S. D., Otaki, M., Jaramillo, R., Podpirka, A., & Ramanathan, S. (2012). Stable metal–insulator transition in epitaxial $SmNiO_3$ thin films. *Journal of Solid State Chemistry*, *190*, 233-237.

[S4] Girardot, C., Kreisel, J., Pignard, S., Caillault, N., & Weiss, F. (2008). Raman scattering investigation across the magnetic and metal-insulator transition in rare earth nickelate R NiO_3 (R= Sm, Nd) thin films. *Physical Review B*, *78*(10), 104101.

[S5] Garcia-Munoz, J. L., Rodriguez-Carvajal, J., Lacorre, P., & Torrance, J. B. (1992). Neutron-diffraction study of R NiO_3 (R= La, Pr, Nd, Sm): Electronically induced structural changes across the metal-insulator transition. *Physical review B*, *46*(8), 4414.

[S6] Lindermeir, E., Haschberger, P., Tank, V., & Dietl, H. (1992). Calibration of a Fourier transform spectrometer using three blackbody sources. *Applied optics*, *31*(22), 4527-4533.

[S7] Mattoni, G., Zubko, P., Maccherozzi, F., van der Torren, A. J., Boltje, D. B., Hadjimichael, M., ... & Aarts, J. (2016). Striped nanoscale phase separation at the metal–insulator transition of heteroepitaxial nickelates. Nature communications, 7, 13141.

[S8] Zhang ZM, Choi BI, Flik MI, Anderson AC (1994). Infrared refractive indices of $LaAlO_3$, $LaGaO_3$, and $NdGaO_3$. *Journal of the Optical Society of America B.*,11(11), 2252-7.

[S9] Mizuno, K., Ishii, J., Kishida, H., Hayamizu, Y., Yasuda, S., Futaba, D. N., ... & Hata, K. (2009). A black body absorber from vertically aligned single-walled carbon nanotubes. Proceedings of the National Academy of Sciences, 106(15), 0900155106.

[S10] Xiao, Y., Shahsafi, A., Roney, P.J., Wan, C., Joe, G., Yu, Z., Salman, J. and Kats, M.A. (2019). Measuring Thermal Emission Near Room Temperature Using Fourier-Transform Infrared Spectroscopy. *Physical Review Applied,* 11(1),014026.

[S11] Schubert, M., Tiwald, T. E., & Herzinger, C. M. (2000). Infrared dielectric anisotropy and phonon modes of sapphire. *Physical Review B*, *61*(12), 8187.

[S12] Weber, M. F., Stover, C. A., Gilbert, L. R., Nevitt, T. J., & Ouderkirk, A. J. (2000). Giant birefringent optics in multilayer polymer mirrors. *Science*, *287*(5462), 2451-2456.